
CellINR: Implicitly Overcoming Photo-induced Artifacts in 4D Live Fluorescence Microscopy

Cunmin Zhao^{1*}, Ziyuan Luo^{1,2*}, Guoye Guan^{3,4*}
 Zelin Li^{5,6}, Yiming Ma¹, Zhongying Zhao¹, Renjie Wan^{1†}

¹ Hong Kong Baptist University ² NVIDIA ³ Harvard Medical School
⁴ Dana-Farber Cancer Institute ⁵ City University of Hong Kong ⁶ CIMDA

*Equal contribution. †Corresponding author.

Abstract

4D live fluorescence microscopy is often compromised by prolonged high intensity illumination which induces photobleaching and phototoxic effects that generate photo-induced artifacts and severely impair image continuity and detail recovery. To address this challenge, we propose the CellINR framework, a case-specific optimization approach based on implicit neural representation. The method employs blind convolution and structure amplification strategies to map 3D spatial coordinates into the high frequency domain, enabling precise modeling and high-accuracy reconstruction of cellular structures while effectively distinguishing true signals from artifacts. Experimental results demonstrate that CellINR significantly outperforms existing techniques in artifact removal and restoration of structural continuity, and for the first time, a paired 4D live cell imaging dataset is provided for evaluating reconstruction performance, thereby offering a solid foundation for subsequent quantitative analyses and biological research. The code and dataset will be public.

1 Introduction

4D live fluorescence microscopy imaging exploits specific wavelengths of light to excite fluorescent markers in biological samples [1], and it acquires 3D image stacks via a computed tomography (CT)-like scanning approach (see Fig. 1a). Subsequently, by capturing these 3D image stacks at uniform time intervals, a 4D live imaging sequence is constructed.

However, compared with conventional imaging methods, 4D live fluorescence imaging requires prolonged repetitive exposures, which subject the sample to continuous high-intensity excitation. This significantly amplifies phototoxicity and photobleaching effects [2–4]. Continuous and high-intensity illumination not only causes irreversible photobleaching of fluorescent probes—resulting in gradual signal decay and a reduction in the image signal-to-noise ratio [5]—but may also induce phototoxic reactions that damage cellular structures and functions, thereby severely impairing the physiological state and dynamic behavior of the cells [6, 7]. These additional noise and artifact issues produced by excessive illumination become particularly pronounced in long-term imaging and high-frequency dynamic monitoring, constituting a major technical barrier to high-precision 4D imaging applications. To address these challenges, various experimental strategies have been devised, such as employing specialized culture media [8, 9], utilizing pulsed excitation [10], and adopting more advanced controlled-illumination microscopy techniques [3, 11]. Moreover, the 4D imaging process often fails to obtain pixel-level matched data, thereby hindering the optimization of imaging results via supervised learning.

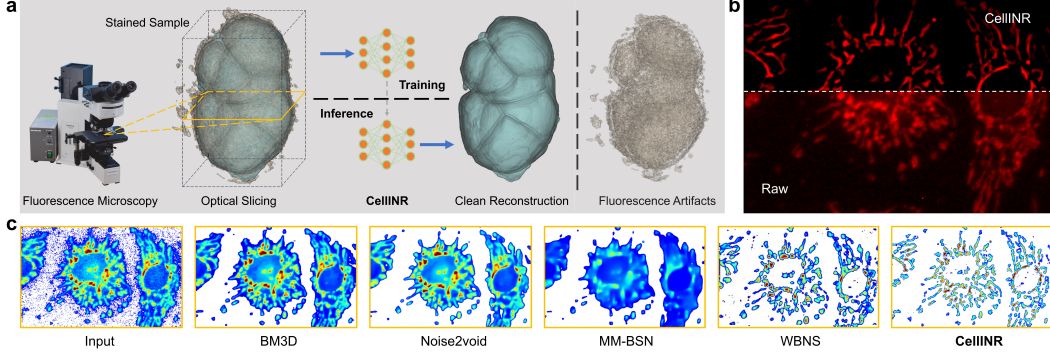


Figure 1: (a) The fluorescence microscope performs 3D imaging through layer-by-layer scanning. Our goal is to remove the photo-induced artifacts in the obtained images. (b) Comparison of raw image and clean reconstruction of BPAE cell samples [12]. (c) Comparative analysis of advanced denoising methods [13–16] with our proposed approach. The denoising results are visualized through heatmap colorization to highlight noise details and demonstrate the performance of different methods.

Furthermore, artifacts exhibit distinct spatiotemporal systematic characteristics, including non-uniform local signal attenuation, time-dependent drift, and prominent structured noise patterns in the images [17, 18]. Currently, most mainstream denoising methods primarily target the inherent random noise of the imaging system (e.g., low photon-count noise and readout noise [12, 14, 19–25]), but they often overlook the pseudo-signals produced by process-dependent photobleaching and phototoxicity under continuous illumination (see Fig. 1c) [26, 27]. Therefore, there is an urgent need to develop novel denoising strategies that both account for the intrinsic noise characteristics of the imaging system and adequately accommodate the dynamic artifact patterns induced by illumination conditions, thereby enabling precise restoration and quantitative analysis of 4D live imaging data.

Fluorescence imaging typically employs a tomographic method to acquire 3D image stacks. Despite the presence of artifacts, the spatial distribution of signals in 3D space exhibits consistency—including both adjacent pixels within different scanning layers and the continuity of signals within the same scanning layer. This adjacent information can be used to eliminate the discontinuities caused by noise [14, 28]. Therefore, our research focus has shifted from directly removing conventional noise to utilizing the overall image structure to clearly reconstruct the target signal from noisy images.

Based on these considerations, we employ Implicit Neural Representation (INR) [29] to model the entire cell structure, as INR demonstrates exceptional efficacy in capturing position-dependent correlations. We optimize the INR on a case-by-case basis using blind convolution [14], which enables a faithful representation of the unique three-dimensional features of each cell structure. Furthermore, its powerful capability to recover information from incomplete data effectively addresses issues of structural discontinuity [30].

To further mitigate the impact of artifact on image reconstruction, we introduce a structure amplification scheme. This approach not only enhances the core cellular structures but also reduces the influence of artifact during the modeling process. These design choices enable INR to more effectively decouple the signal from the artifact while maintaining continuity and detail accuracy in the reconstructed image (see Figure 1b). Additionally, we have constructed a paired 4D noise dataset for evaluating denoising performance, and we have validated the robustness of our denoising approach on several unpaired public datasets. Our major contribution can be concluded as follows:

1. **CellINR**, an INR-based case-specific optimization framework, effectively recovers the core cell structures from 4D fluorescence images through self-supervised methods.
2. We optimize the INR reconstruction process using blind convolution and structure amplification, constructing clear 3D representations of noisy fluorescence images through a complete forward propagation process.
3. We have constructed a paired dataset of 3D images acquired under both low-exposure and high-exposure conditions, as well as a synthetic dataset for 4D imaging. In addition, we have also collected an unpaired dataset containing background artifacts. Extensive

experimental results demonstrate that CellINR significantly outperforms state-of-the-art methods in eliminating photo-induced artifacts.

We optimize each cell’s INR to ensure the representation closely aligns with actual measurements. Once optimization is complete, we can accurately recover and visualize cell structures at their corresponding locations for biological analysis.

2 Related work

Implicit Neural Representations (INR). Implicit neural representations typically use a multi-layer perceptron (MLP) to map local coordinates to their corresponding values [29, 31], such as pixel intensities for images or occupancy values for 3D volumes. An overview of INR fundamentals is provided below. An INR is a neural network $F_\theta : \mathbf{x} \mapsto F_\theta(\mathbf{x})$ that continuously maps coordinates \mathbf{x} to the desired quantity. Given data expressed as a function $\Phi : \mathbf{x} \mapsto \Phi(\mathbf{x})$, the INR F_θ aims to solve $F_\theta(\mathbf{x}) - \Phi(\mathbf{x}) = 0$. The weights θ of the INR are typically found through optimization. INRs have proven effective in parameterizing geometry and learning shape priors, as seen in DeepSDF [32], Occupancy Networks [33], and IM-Net [34]. Many subsequent works have proposed volumetric rendering techniques for 3D implicit representations, including Neural Radiance Fields (NeRF) [35] and its variants for faster rendering [36, 37], sparse reconstruction [38, 39], and improved quality [40, 41]. Recent advancements include CuNeRF [42], which achieves zero-shot super-resolution at arbitrary scales. McGinnis et al. [43] improved multi-contrast MRI imaging using implicit representations. While Kniesel et al. [44] reconstructed 3D structures from STEM images by modeling mechanical noise, their method struggles with local accidental excitation fluorescence noise. Though NeRF and its variants excel in 3D reconstruction, further research is needed to address complex artifacts in fluorescence microscopy super-resolution.

Fluorescence Image Denoising. Based on the statistical characteristics of optical imaging noise, researchers modeled noisy images as the superposition of deterministic signals and independent Poisson-Gaussian distributions [12, 45]. Traditional denoising methods such as Non-Local Means (NLM) [46] and wavelet transforms [47] have been widely applied in biological imaging. Dabov et al. [13] proposed a sparse three-dimensional transform-domain collaborative filtering algorithm, achieving remarkable results in Gaussian noise suppression. With the rapid development of deep learning technology, supervised learning-based denoising methods have demonstrated superior performance in learning complex noise patterns and achieving higher quality image reconstruction [20, 48, 49]. However, their dependence on high-quality annotated data limits their application in biological imaging. Recently, unsupervised learning algorithms have made breakthrough progress in image denoising: Noise2void [14] achieve self-supervised denoising using blind convolution; methods such as Noisier2Noise and Recorrupted-to-recorrupted [50, 51] enable training with unpaired noisy data by introducing enhanced noise. These algorithms excel in diverse noise environments. However, for background artifacts removal, traditional techniques [16, 52, 53] remain the most effective.

Preliminaries

Fluorescence microscopy images can be modeled as the sum of the true signal and various noise components [1]:

$$I(x, y, z) = P \otimes S(x, y, z) + N_{\text{conv}}(x, y, z) + N_{\text{artifacts}}(x, y, z), \quad (1)$$

where P denotes the point spread function, $I(x, y, z)$ is the observed image, and $S(x, y, z)$ is the ideal fluorescence signal. $N_{\text{conv}}(x, y, z)$ represents conventional noise (e.g., from photon scarcity and vibrations), typically following a Poisson–Gaussian distribution that is either uniform or signal-dependent.

In contrast, $N_{\text{artifacts}}(x, y, z)$ represents artifacts induced by photobleaching and phototoxicity, arising from signal degradation and complex biological interference [13, 28, 46, 54]. Fluorescence signals are usually localized in specific structures (e.g., membranes and nuclei) and exhibit high-frequency features, whereas artifacts tend to be uniformly low-frequency [17, 18]. This distinction forms the basis for designing targeted artifact removal methods to separate structured signals from noise.

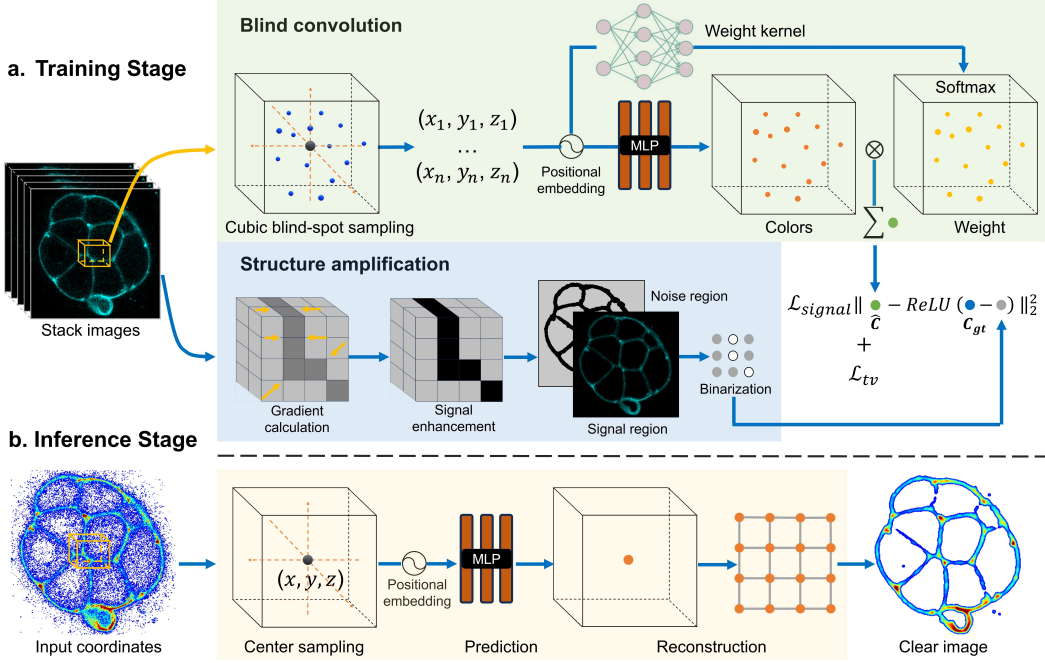


Figure 2: Overview of the CellINR framework. (a) Training Stage: Cubic blind-spot sampling is performed on noisy images, with MLP predicting sample point colors, and blind deconvolution with structure amplification reconstructing center pixel values. (b) Inference Stage: Spatial coordinates of target pixels are sampled to output clear reconstruction results.

3 Proposed methodology

As shown in Fig.2a, CellINR adopts a case-by-case optimization strategy to construct clear 3D representations from fluorescence images during INR’s forward propagation. During training, cubic sampling randomly selects multiple sampling points around each target pixel and performs convolution summation to eliminate noise interference to ensure signal smoothness and robust noise suppression. Meanwhile, structural amplification is applied to fluorescence images to eliminate jagged effects at signal boundaries and locally uniform low-brightness distribution of artifacts. During inference stage, INR is directly sampled to generate clear continuous 3D representation.

3.1 CellINR

The backbone of our CellINR uses a Multi-Layer Perceptron (MLP) [55] with parameters ϱ to map spatial coordinates ρ of fluorescence images to their corresponding implicit expressions. We perform uniform sampling in the fluorescence image space to obtain N discrete coordinate points ρ , denoted as N_ρ . Subsequently, we map the coarse sampling point set N_ρ to high-frequency domain space to enhance the model’s ability to capture details [35], represented here as:

$$\gamma(\rho) = [\sin(\rho), \cos(\rho), \dots, \sin(2^{\epsilon-1}\rho), \cos(2^{\epsilon-1}\rho)]^T, \quad (2)$$

where ϵ represents the dimension of positional encoding. Through simple mapping, we obtain:

$$c = F_\varrho(\gamma(\rho)), \quad (3)$$

where c is the color value of the pixel at spatial position ρ in the implicit representation. However, INR constructed through this method alone tends to behave as identity mappings, failing to effectively model clear representations of fluorescence images.

3.2 Blind convolution

Based on the discrete nature of photo-induced artifacts and continuous distribution characteristics of signal features, we recognize that noise disrupts continuity between adjacent pixels. Meanwhile,

fluorescence signal distribution maintains structural continuity within regions. Inspired by [14, 45], we model 3D continuous representations of fluorescence images using INR based on 3D blind-spot convolution. This method estimates target point values through the convolution of points around the target pixel while ensuring noise information from target pixels is not input to the neural network. Traditional 3D blind-spot convolution can be represented as:

$$I_{(x,y,z)} = \sum_{i=-h}^h \sum_{j=-h}^h \sum_{k=-h}^h C_{x-i,y-j,z-k} \cdot W_{x-i,y-j,z-k}, \quad (4)$$

where $C_{x-i,y-j,z-k}$ represents the pixel value of sampling points with coordinate offset (i, j, k) within a cubic space centered at point (x, y, z) with radius h , $W_{x-i,y-j,z-k}$ is the weight convolution kernel corresponding to each pixel position, and $I_{(x,y,z)}$ is the pixel value at position (x, y, z) obtained after convolution operation between C and W , used to estimate the pixel value at the target point in noise-free conditions. To avoid blind spot invalidation caused by target pixels being input to the network during convolution [45], and to maintain INR continuity while preventing mesh artifacts and modeling holes during sampling [42], we improved INR's sampling method to approximate the convolution kernel.

Specifically, we perform random coarse sampling on spatial coordinates in S_{cube} to obtain N discrete coordinate points, denoted as N_c . Subsequently, we input the positionally encoded coarse sampling points into coarse MLP F_Θ to predict volume density $\sigma = F_\Theta(\gamma(N_c))$. Based on the predicted volume density, we construct a cumulative distribution function (CDF) and apply importance sampling strategy [42], sampling N_f fine sampling points $N_f = \xi(N_c, \sigma)$. Here, ξ is the function performing fine sampling based on the volume density $\sigma(N_c)$ of coarse sampling points. Merging coarse sampling point set N_c with fine sampling point set N_f , we obtain the final sampling point set $N_{(x,y,z)} = N_c \cup N_f$, where N represents the blind-spot cube sampling point set centered at (x, y, z) . Then, the merged sampling point set is input to fine MLP F_δ to predict corresponding color values:

$$c(\rho) = F_\delta[\gamma(\rho \cup \xi(\rho, F_\Theta[\gamma(\rho)]))], \quad \text{where } \rho \in N. \quad (5)$$

Considering that convolution kernel weights are typically spatially varying in complex noisy images, we choose to use MLP F_ϕ to model spatially varying kernels. To ensure weight normalization, we apply the Softmax function to generated weights, making their sum equal to 1. Specifically, for each input view, we predict the weights as:

$$w(\rho) = \frac{\exp(F_\phi(\gamma(\rho)))}{\sum_{\rho \in N} \exp(F_\phi(\gamma(\rho)))}. \quad (6)$$

Finally, our blind convolution can be expressed as:

$$I_{\text{clean}} = \sum_{\rho \in N} [c(\rho) \cdot w(\rho)], \quad (7)$$

This method effectively models continuous representations of fluorescence images in INR.

3.3 Structural amplification

Another characteristic of photo-induced artifact is its uniform low-frequency distribution in local regions[17, 18]. In contrast, the features of the fluorescence signal are confined to specific cellular structures and generally exhibit a concentrated high-frequency distribution. To further suppress photo-induced artifact, a Hessian matrix enhancement technique is applied to the input image [56–58]. to input images. Specifically, we calculate second-order partial derivatives of images and perform eigenvalue decomposition to select pixels conforming to planar structures, thereby enhancing fluorescent feature signals. For a 3D fluorescence image $I^f(x, y, z)$, we compute the Hessian matrix as:

$$H = \begin{bmatrix} \frac{\partial^2 I^f}{\partial x^2} & \frac{\partial^2 I^f}{\partial x \partial y} & \frac{\partial^2 I^f}{\partial x \partial z} \\ \frac{\partial^2 I^f}{\partial x \partial y} & \frac{\partial^2 I^f}{\partial y^2} & \frac{\partial^2 I^f}{\partial y \partial z} \\ \frac{\partial^2 I^f}{\partial x \partial z} & \frac{\partial^2 I^f}{\partial y \partial z} & \frac{\partial^2 I^f}{\partial z^2} \end{bmatrix} = E \Lambda E^T, \quad (8)$$

where $\lambda_1, \lambda_2, \lambda_3$ are the eigenvalues satisfying $|\lambda_1| < |\lambda_2| < |\lambda_3|$, and e_1, e_2, e_3 are the corresponding eigenvectors. By selecting the largest eigenvalue λ_3 , we enhance the fluorescent signals:

$$I_{\text{en}}(x, y, z) = \frac{|\lambda_3(x, y, z)|}{\max\{|\lambda_3(x, y, z)| \mid x, y, z \in I\}}. \quad (9)$$

The enhanced image I_{en} is then binarized, assigning signal regions a value of 255 and noise regions a value of 0, resulting in a binary image I_{binary} . The binarization process is represented as:

$$I_{\text{binary}}(x, y, z) = \begin{cases} 255, & \text{if } I_{\text{en}}(x, y, z) > \mu, \\ 0, & \text{otherwise,} \end{cases} \quad (10)$$

where μ is the Otsu thresholding[59] of the largest eigenvalues.

3.4 Loss function

To effectively train the CellINR framework, we design a hybrid three-dimensional loss function that optimizes the reconstruction effect in signal regions while maintaining the three-dimensional structural consistency of the image. The loss function primarily consists of two components.

Clean reconstruction loss: For pixel points labeled as signal regions based on the binarized image I_{binary} , we calculate the MSE between the reconstructed image I_{clean} and the rectified original noisy image I_{raw} activated by ReLU:

$$\mathcal{L}_{\text{signal}} = \frac{1}{N} \sum_I (I_{\text{clean}} - \text{ReLU}(I_{\text{raw}} - I_{\text{binary}}))^2, \quad (11)$$

where N represents the total number of pixel points in the signal regions, and $\text{ReLU}(x) = \max(0, x)$ ensures that only the signal regions contribute to the error calculation.

Structural consistency loss: To enhance the structural consistency of the reconstructed image, we introduce a Structural Consistency Loss based on the Total Variation (TV) method. Here, X represents the pixel matrix of the reconstructed image, while i and j denote the horizontal and vertical pixel indices, respectively. The TV loss is defined as

$$\mathcal{L}_{\text{TV}}(X) = \sum_{i,j} (|X_{i+1,j} - X_{i,j}| + |X_{i,j+1} - X_{i,j}|). \quad (12)$$

This loss function encourages smooth transitions between adjacent pixels, thereby suppressing artifacts and noise, and ultimately enhancing the continuity of the image structure.

Combining these two components, the final total loss is defined as:

$$\mathcal{L} = \mathcal{L}_{\text{signal}} + \lambda \mathcal{L}_{\text{TV}}, \quad (13)$$

where λ is a balancing coefficient, set to 0.15 in our experiments. This loss function enables CellINR to maintain detailed signal regions while ensuring three-dimensional structural consistency, achieving high-quality image denoising and clean reconstruction.

3.5 Implementation details

We implemented the CellINR framework based on NeRF’s PyTorch implementation [60], CuNeRF [42] and Deblur-NeRF [61]. The specific settings are as follows: within a cubic space of radius 1 around the blind spot, $N = 27$ coordinate points are uniformly sampled during experiments, inputting coarse predictions of volume density via F_{θ} . In the fine volume, an additional N coordinate points are sampled, totaling $2N$ points input into the fine F_{δ} and kernel modules to output color values and corresponding weights. To ensure that the kernel module outputs only weights, a Softmax function is applied to ensure the sum of the $2N$ weights equals 1. The optimizer used is Adam with a weight decay of 10^{-6} , a batch size of 4096, a maximum of 500,000 iterations, and a learning rate linearly annealing from 2×10^{-3} to 2×10^{-5} . Training one (256,356,160) volume image on a single NVIDIA RTX 4090 GPU required 50,000 iterations, 20 minutes. The MLP structure is identical to NeRF, comprising 8 fully connected hidden layers with 256 channels each and ReLU activation functions. The kernel module follows a similar structure, with center point coordinates input to the seventh layer to assist in weight generation. The specific architecture is detailed in *Supplementary materials*. During inference stage (Fig.2b), the fine F_{δ} predicts the corresponding pixel values using center point coordinates, and kernel weights are set to 1. By varying sampling densities, output images at different resolution can be obtained.

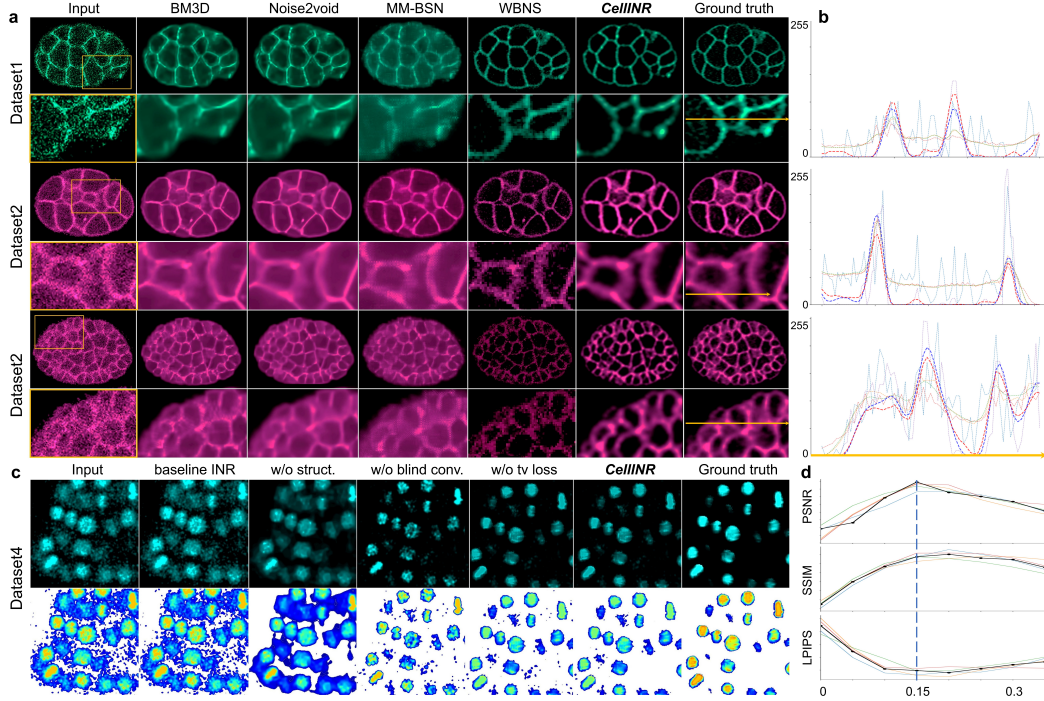


Figure 3: Visual comparison with existing methods. (a) Visualization of the benchmark on Dataset 1 and Dataset 2. (b) Distribution of pixel values along selected line segments for different methods. The curves are color-coded as follows: **Input**, **BM3D**, **Noise2Void**, **MM-BSN**, **WBNS**, **CellINR**, and **Ground Truth**. (c) Visualization of ablation experiments on Dataset 3. (d) Sensitivity test of the hyperparameter λ in structural consistency loss.

4 Experiments

4.1 Datasets

Dataset	Model system	Excitation	Type	Exposure Time	Number	Image Size	Source	GT
dataset1	C.elegans cell membrane	561nm	Static 3D Imaging	176s	40		paired real dataset	
dataset2	C.elegans cell membrane	561nm	Time-Resolved 3D Imaging	176s	40			
dataset3	C.elegans cell membrane	561nm	Time-Resolved 3D Imaging	752s	80	(256,356,214)	Ours	paired synthetic dataset
dataset4	C.elegans cell nucleus	488nm	Time-Resolved 3D Imaging	176s	40			
dataset5	C.elegans cell membrane	561nm	Time-Resolved 3D Imaging	/	40	(256,356,160)	[62]	
dataset6	BAPE	/	Static 2D Imaging	/	20	(512,512)	[12]	
dataset7	Zerbafish	/	Static 2D Imaging	/	20	(512,512)	[12]	unpaired dataset
dataset8	Mouse	/	Static 2D Imaging	/	2	(299,298)	[63]	

Table 1: The composition of the qualitative/quantitative datasets used in this study to evaluate the denoising results.

In this study, datasets 1, 2, 3, and 4 were acquired from live *C. elegans* embryo imaging using a Leica SP5II confocal microscope equipped with a $63\times/1.4$ NA objective lens. The embryos were placed on a 3–5% (w/v) agarose pad, treated with 0.5% tetramisole, and sealed with vaseline. Datasets 1, 2, and 3 were labeled with mCherry to mark the cell membrane and excited by a 561 nm laser, whereas dataset 4 employed green fluorescent protein (GFP) to label the cell nucleus and was excited by a 488 nm laser. All four datasets have a resolution of 712×512 pixels in the xy plane, with 44, 44, 94, and 44 focal planes acquired along the z -axis, respectively (the xy resolution is $0.09\ \mu\text{m}/\text{pixel}$, and the z resolutions are 0.42 , 0.42 , 0.24 , and $0.42\ \mu\text{m}/\text{pixel}$, respectively). Dataset 1 is a static paired dataset obtained under low- and high-illumination conditions. By controlling the exposure time of individual 2D slices (10 ms for the low-exposure, low-SNR group and 100 ms for the high-exposure, high-SNR group), 20 paired groups of low-noise and high-noise images were obtained, yielding a total of 40 image sets. Datasets 2 to 4 are time-resolved 3D imaging datasets acquired with an exposure time of 100 ms per 2D slice and sampled repeatedly from a single embryo at 90-second intervals.

Benchmark	Dataset1			Dataset2			Dataset4			
	PSNR↑	SSIM↑	LPIPS↓	PSNR↑	SSIM↑	LPIPS↓	PSNR↑	SSIM↑	LPIPS↓	
Comparison	BM3D (Traditional)	22.737±3.27	0.678±0.086	0.170±0.022	20.630±3.06	0.718±0.027	0.111±0.016	19.936±2.00	0.757±0.067	0.158±0.021
	Noise2void (Self-supervised)	22.815±2.28	0.618±0.066	0.137±0.019	21.466±3.15	0.759±0.095	0.118±0.017	18.554±1.86	0.735±0.074	0.147±0.019
	MM-BSN (Self-supervised)	21.408±2.14	0.599±0.045	0.233±0.028	20.416±2.04	0.659±0.067	0.197±0.025	18.809±1.88	0.665±0.066	0.283±0.022
	WBNS (Traditional)	33.180±1.66	0.842±0.042	0.141±0.007	34.898±1.75	0.904±0.045	0.037±0.002	32.698±1.64	0.902±0.045	0.033±0.002
Ablation	baseline INR	23.804±3.38	0.526±0.079	0.259±0.021	23.302±3.32	0.681±0.096	0.209±0.010	20.869±3.97	0.578±0.047	0.242±0.011
	w/o blideconv.	30.040±3.40	0.826±0.053	0.159±0.013	32.210±2.22	0.831±0.058	0.109±0.015	30.640±3.54	0.878±0.078	0.100±0.012
	w/o struct.	27.730±2.37	0.751±0.057	0.137±0.010	22.230±3.22	0.619±0.062	0.172±0.012	21.550±2.76	0.723±0.072	0.175±0.012
	w/o TV loss	33.460±3.35	0.868±0.087	0.129±0.014	37.640±3.76	0.913±0.091	0.053±0.007	33.020±3.30	0.900±0.090	0.050±0.004
CellINR (Self-supervised)										
35.470±1.77 0.881±0.044 0.079±0.004 38.620±1.93 0.925±0.046 0.029±0.001 33.170±1.66 0.919±0.046 0.025±0.001										

Table 2: Quantitative comparison of PSNR, SSIM, and LPIPS across three datasets. CellINR scores are highlighted in **orange** and WBNS scores in **cyan** (indicating the best and second best performance, respectively). Mean±std is reported for each metric.

Specifically, datasets 2 and 4 each include 40 time points (with cumulative exposure times of 176 s, respectively), while dataset 3 comprises 80 time points (with a cumulative exposure time of 752 s). After processing with Leica LAS X software and ImageJ, the images were resampled using trilinear interpolation to achieve a uniform resolution of $0.18 \mu\text{m}/\text{pixel}$ in all three dimensions, ultimately yielding 200 sets of 3D NIFTI data with dimensions (256, 356, 214). Dataset 1 is primarily used to evaluate denoising performance under low-light conditions and is constructed based on the prominent photo-induced artifacts observed in the long-exposure 4D dataset 3. To simulate the photo-induced artifacts encountered in live fluorescence microscopy, Poisson noise (factor = 0.1) and Gaussian noise (with a standard deviation of 20 added to non-zero pixel regions) were incorporated into datasets 2 and 4, respectively. For quantitative evaluation, the paired datasets consist of datasets 1, 2, and 4 (comprising 20, 40, and 40 pairs, respectively), while datasets 3, 5 [62], 6 [12], 7 [12], and 8 [63] are used solely for qualitative evaluation; corresponding experimental results are provided in the supplementary material.

4.2 Quantitative Evaluation

To assess denoising performance, we compared CellINR with mainstream denoising models[13–16]. These methods were applied to datasets 1, 2, and 4 (visual results are shown in Fig. 3a and quantitative results in Table 2). All methods were implemented using the open-source codes provided by the respective authors. A comprehensive visual comparison reveals that CellINR offers significant advantages in removing photo-induced artifacts. In terms of suppressing jagged edges at microscopic structures, eliminating pseudo-signals, and overall reconstruction quality, CellINR provides the best interpretation of cellular structural signals. Specifically, CellINR successfully eliminates artifacts that are difficult for mainstream denoising methods. Although WBNS can remove some artifacts, its wavelet decomposition process inevitably disrupts signal continuity; in contrast, CellINR accurately reconstructs the continuous signal structure within the noise, preserving the integrity of fine cellular features without introducing aliasing. Figure 3b shows the pixel intensity profiles along a yellow line for three samples denoised by different methods, where the CellINR result closely matches the ground truth with minimal artifacts. For denoising results on datasets 3, 5, 6, 7, and 8, please refer to the supplementary material. For the three paired datasets, we conducted a comprehensive evaluation using PSNR, SSIM, and LPIPS metrics, repeating experiments on all data within each dataset and reporting the mean and standard deviation. In the real 3D dataset (dataset 1), CellINR not only showed approximately a 30% improvement in mean values over other mainstream denoising methods (approximately 10% improvement over WBNS) but also exhibited higher robustness in fine detail restoration, with minimal standard deviation in all metrics. In the synthetic 4D datasets (datasets 2 and 4), CellINR also demonstrated stable and excellent quantitative performance, confirming its suitability for removing photo-induced artifacts in live fluorescence microscopy under unsupervised conditions.

4.3 Ablation Experiments

To further quantitatively assess the effectiveness of each component in CellINR framework, we conducted ablation experiments using the same evaluation metrics and datasets as in the quantitative evaluation. We compared variants in which only the baseline INR is employed, the blind convolution module is removed, the structural amplification module is removed, or the TV loss is omitted against the complete CellINR model. Using only the baseline INR resulted in the model behaving

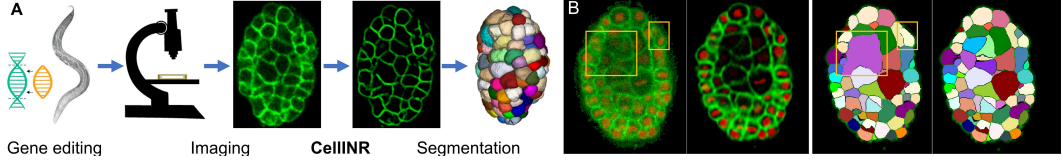


Figure 4: (a) Cell morphology modeling using 4D live fluorescence microscopy during *Caenorhabditis elegans* embryonic development. (b) Segmentation results before and after denoising. The yellow box shows that artifact removal reduces misidentification in downstream analysis.

essentially as an identity mapping, consistent with the discussion in Section 4.1, and it performed significantly worse across all metrics. Removal of the blind convolution module led to a marked decline in the ability to maintain signal continuity and anti-aliasing at edges, underscoring its critical role in constructing a continuous representation. Eliminating the structural amplification module significantly reduced the model’s capacity to remove artifacts—especially low-frequency background pseudo-signals—with experimental results showing an approximate PSNR drop of 10 dB and a SSIM decrease of about 0.2, thereby demonstrating the necessity of incorporating artifact-based structural amplification during training. Omitting the TV loss slightly decreased both PSNR and SSIM, indicating a weakened suppression of high-frequency noise and isolated noise points, which confirms the importance of smoothing for signal optimization. Detailed quantitative results for the ablation experiments are provided in Table 1.

4.4 Downstream Tasks

The results of 4D live fluorescence microscopy are often used for subsequent downstream analyses to obtain time-series 3D shapes, which serve as the basis for physical modeling and studies in quantitative biology and developmental biology [62, 64–66]. In this study, we employed gene editing to label the cell membrane and nucleus with fluorescent proteins and performed 3D segmentation for quantitative analysis of cellular morphology (see Fig. 4a). The 3D segmentation pipeline follows a standard procedure: first, Mask-RCNN [67] was used for automatic segmentation of the nuclei and to extract their centroids as seeds; subsequently, an avascular enhancement filter [68] (with scale parameters set sequentially to 2.0, 2.25, and 2.5) was applied to amplify the boundary signals in the cell membrane region, followed by a seeded watershed algorithm to accurately extract cell contours, thus obtaining the complete cell shape; finally, manual corrections were performed using Labkit to refine the edge details and ensure the segmentation results closely match the actual cellular morphology. As shown in Fig. 4b, artifact removal significantly reduced blurred regions, and the cell membrane structures became clearer with enhanced boundary signals. This effectively reduced errors such as signal misrecognition and segmentation inaccuracies caused by artifacts in downstream tasks, thereby greatly improving the accuracy of subsequent analyses.

Conclusion

This study presents the **CellINR** framework based on implicit neural representations, which systematically integrates blind convolution and structural amplification strategies to effectively suppress photo-induced artifacts and accurately restore the continuity of cellular structures in 4D live fluorescence microscopy. The proposed method has achieved notable success in noise optimization and the recovery of critical structures, thereby providing high-quality data support for quantitative analyses of embryonic development, cell differentiation, and other dynamic biological processes. Rigorous quantitative experiments confirm that CellINR meets the stringent requirements for precise capture of fine structures in biological imaging, thereby establishing a robust theoretical and practical foundation for multi-scale and multi-modal biological information analysis. However, CellINR may misclassify data where artifacts and genuine signals are ambiguous; thus, it is best applied to datasets with clearly distinguishable artifacts. Additionally, for multi-channel composite images, processing without separate single-channel data may conflate fluorescence signals and compromise reconstruction quality. Future work will further incorporate biophysical models to extend its applicability in complex biological systems.

References

- [1] J. Mertz. *Introduction to Optical Microscopy*, pages 142–160. Cambridge University Press, 2019. [1](#) [3](#)
- [2] J. Y. Tinevez, J. Dragavon, L. Baba-Aissa, P. Roux, E. Perret, A. Canivet, and S. Shorte. A quantitative method for measuring phototoxicity of a live cell imaging microscope. In *Methods in Enzymology*, volume 506, pages 291–309. Academic Press, 2012. [1](#)
- [3] R. A. Hoebe, C. H. Van Oven, T. W. J. Gadella, et al. Controlled light-exposure microscopy reduces photobleaching and phototoxicity in fluorescence live-cell imaging. *Nature Biotechnology*, 25:249–253, 2007. [1](#)
- [4] R. A. Hoebe, H. T. M. Van Der Voort, J. Stap, C. J. F. Van Noorden, and E. M. M. Manders. Quantitative determination of the reduction of phototoxicity and photobleaching by controlled light exposure microscopy. *Journal of Microscopy*, 231(1):9–20, 2008. [1](#)
- [5] C. Eggeling, J. Widengren, R. Rigler, and C. A. Seidel. Photobleaching of fluorescent dyes under conditions used for single-molecule detection: evidence of two-step photolysis. *Analytical Chemistry*, 70(13):2651–2659, 1998. [1](#)
- [6] A. H. Wright, J. M. DeLong, J. L. Franklin, R. R. Lada, and R. K. Prange. A new minimum fluorescence parameter, as generated using pulse frequency modulation, compared with pulse amplitude modulation: f_α versus f_0 . *Photosynthesis Research*, 97:205–214, 2008. [1](#)
- [7] R. Dixit and R. Cyr. Cell damage and reactive oxygen species production induced by fluorescence microscopy: effect on mitosis and guidelines for non-invasive fluorescence microscopy. *The Plant Journal*, 36(2):280–290, 2003. [1](#)
- [8] A. M. Bogdanov, E. A. Bogdanova, D. M. Chudakov, et al. Cell culture medium affects gfp photostability: A solution. *Nature Methods*, 6:859–860, 2009. [1](#)
- [9] A. M. Bogdanov, E. I. Kudryavtseva, and K. A. Lukyanov. Anti-fading media for live cell gfp imaging. *PLoS One*, 7:e53004, 2012. [1](#)
- [10] T. Nishigaki, C. D. Wood, K. Shiba, et al. Stroboscopic illumination using light-emitting diodes reduces phototoxicity in fluorescence cell imaging. *Biotechniques*, 41:191–197, 2006. [1](#)
- [11] W. Caarls, B. Rieger, A. H. B. De Vries, et al. Minimizing light exposure with the programmable array microscope. *Journal of Microscopy*, pages 101–110, 2010. [1](#)
- [12] Y. Zhang, Y. Zhu, E. Nichols, Q. Wang, S. Zhang, C. Smith, and S. Howard. A poisson-gaussian denoising dataset with real fluorescence microscopy images. In *Proceedings of the IEEE/CVF Conference on Computer Vision and Pattern Recognition*, pages 11710–11718, 2019. [2](#) [3](#) [7](#) [8](#)
- [13] K. Dabov, A. Foi, V. Katkovnik, and K. Egiazarian. Image denoising by sparse 3-d transform-domain collaborative filtering. *IEEE Transactions on Image Processing*, 16(8):2080–2095, 2007. [2](#) [3](#) [8](#)
- [14] A. Krull, T. O. Buchholz, and F. Jug. Noise2void—learning denoising from single noisy images. In *Proceedings of the IEEE/CVF Conference on Computer Vision and Pattern Recognition*, pages 2129–2137, 2019. [2](#) [3](#) [5](#)
- [15] D. Zhang, F. Zhou, Y. Jiang, and Z. Fu. Mm-bsn: Self-supervised image denoising for real-world with multi-mask based on blind-spot network. In *Proceedings of the IEEE/CVF Conference on Computer Vision and Pattern Recognition*, pages 4189–4198, 2023.
- [16] M. Hüpfel, A. Yu. Kobitski, W. Zhang, and G. U. Nienhaus. Wavelet-based background and noise subtraction for fluorescence microscopy images. *Biomedical Optics Express*, 12(2):969–980, 2021. [2](#) [3](#) [8](#)
- [17] J. Icha, M. Weber, J. C. Waters, and C. Norden. Phototoxicity in live fluorescence microscopy, and how to avoid it. *BioEssays*, 39(8):1700003, 2017. [2](#) [3](#) [5](#)
- [18] P. P. Laissue, R. A. Alghamdi, P. Tomancak, E. G. Reynaud, and H. Shroff. Assessing phototoxicity in live fluorescence imaging. *Nature Methods*, 14(7):657–661, 2017. [2](#) [3](#) [5](#)
- [19] Ernst H K Stelzer. Contrast, resolution, pixelation, dynamic range and signal-to-noise ratio: fundamental limits to resolution in fluorescence light microscopy. *Journal of Microscopy*, 189(1):15–24, 1998. [2](#)
- [20] Kai Zhang, Wangmeng Zuo, Yunjin Chen, Deyu Meng, and Lei Zhang. Beyond a Gaussian denoiser: Residual learning of deep CNN for image denoising. *IEEE Transactions on Image Processing*, 26(7):3142–3155, 2017. [3](#)

[21] Martin Weigert, Uwe Schmidt, Tobias Boothe, et al. Content-aware image restoration: pushing the limits of fluorescence microscopy. *Nature Methods*, 15:1090–1097, 2018. doi: 10.1038/s41592-018-0216-7.

[22] Tobias Plotz and Stefan Roth. Benchmarking denoising algorithms with real photographs. In *Proceedings of the IEEE Conference on Computer Vision and Pattern Recognition (CVPR) Workshops*, pages 99–107, 2017.

[23] Jaakko Lehtinen, Joakim Munkberg, Jon Hasselgren, Samuli Laine, Tero Karras, Miika Aittala, and Timo Aila. Noise2noise: Learning image restoration without clean data. In *Proceedings of the 35th International Conference on Machine Learning (ICML)*, 2018.

[24] J. Batson and L. Royer. Noise2self: Blind denoising by self-supervision. In *International Conference on Machine Learning*, pages 524–533. PMLR, 2019.

[25] Jonathan Ho, Ajay Jain, and Pieter Abbeel. Denoising diffusion probabilistic models. In *Advances in Neural Information Processing Systems*, volume 33, pages 6840–6851, 2020. [2](#)

[26] M. Guo, Y. Wu, C.M. Hobson, et al. Deep learning-based aberration compensation improves contrast and resolution in fluorescence microscopy. *Nat Commun*, 16:313, 2025. doi: 10.1038/s41467-024-55267-x. URL <https://doi.org/10.1038/s41467-024-55267-x>. [2](#)

[27] G. M. Hagen, J. Bendesky, R. Machado, T. A. Nguyen, T. Kumar, and J. Ventura. Fluorescence microscopy datasets for training deep neural networks. *GigaScience*, 10(5):giab032, 2021. [2](#)

[28] C. Qiao, Y. Zeng, Q. Meng, X. Chen, H. Chen, T. Jiang, and Q. Dai. Zero-shot learning enables instant denoising and super-resolution in optical fluorescence microscopy. *Nature Communications*, 15(1):4180, 2024. [2](#), [3](#)

[29] Vincent Sitzmann, Julien Martel, Alexander Bergman, David Lindell, and Gordon Wetzstein. Implicit neural representations with periodic activation functions. In *Advances in Neural Information Processing Systems*, volume 33, pages 7462–7473. NeurIPS, 2020. [2](#)

[30] A. Molaei, A. Aminimehr, A. Tavakoli, A. Kazerouni, B. Azad, R. Azad, and D. Merhof. Implicit neural representation in medical imaging: A comparative survey. In *Proceedings of the IEEE/CVF International Conference on Computer Vision*, pages 2381–2391, 2023. [2](#)

[31] Daniele Grattarola and Pierre Vandergheynst. Generalised implicit neural representations. In *Advances in Neural Information Processing Systems*, 2022. [3](#)

[32] Jeong Joon Park, Peter Florence, Julian Straub, Richard Newcombe, and Steven Lovegrove. Deepsdf: Learning continuous signed distance functions for shape representation. In *Proceedings of the IEEE/CVF Conference on Computer Vision and Pattern Recognition*, 2019. [3](#)

[33] Lars Mescheder, Michael Oechsle, Michael Niemeyer, Sebastian Nowozin, and Andreas Geiger. Occupancy networks: Learning 3D reconstruction in function space. In *Proceedings of the IEEE/CVF Conference on Computer Vision and Pattern Recognition*, 2019. [3](#)

[34] Zhiqin Chen and Hao Zhang. Learning implicit fields for generative shape modeling. In *Proceedings of the IEEE/CVF Conference on Computer Vision and Pattern Recognition*, 2019. [3](#)

[35] B. Mildenhall, P. P. Srinivasan, M. Tancik, J. T. Barron, R. Ramamoorthi, and R. Ng. Nerf: Representing scenes as neural radiance fields for view synthesis. *Communications of the ACM*, 65(1):99–106, 2021. [3](#), [4](#)

[36] Thomas Müller, Alex Evans, Christoph Schied, and Alexander Keller. Instant neural graphics primitives with a multiresolution hash encoding. *ACM Transactions on Graphics (ToG)*, 2022. [3](#)

[37] Anpei Chen, Zexiang Xu, Andreas Geiger, Jingyi Yu, and Hao Su. TensoRF: Tensorial radiance fields. In *Proceedings of the European Conference on Computer Vision*, 2022. [3](#)

[38] A. Yu, V. Ye, M. Tancik, and A. Kanazawa. Pixelnerf: Neural radiance fields from one or few images. In *Proceedings of the IEEE/CVF Conference on Computer Vision and Pattern Recognition*, pages 4578–4587, 2021. [3](#)

[39] Q. Wang, Z. Wang, K. Genova, P. P. Srinivasan, H. Zhou, J. T. Barron, and T. Funkhouser. Ibrnet: Learning multi-view image-based rendering. In *Proceedings of the IEEE/CVF Conference on Computer Vision and Pattern Recognition*, pages 4690–4699, 2021. [3](#)

[40] J. T. Barron, B. Mildenhall, M. Tancik, P. Hedman, R. Martin-Brualla, and P. P. Srinivasan. Mip-nerf: A multiscale representation for anti-aliasing neural radiance fields. In *Proceedings of the IEEE/CVF International Conference on Computer Vision*, pages 5855–5864, 2021. [3](#)

[41] Jonathan T Barron, Ben Mildenhall, Dor Verbin, Pratul P Srinivasan, and Peter Hedman. Zip-NeRF: Anti-aliased grid-based neural radiance fields. In *Proceedings of the IEEE/CVF International Conference on Computer Vision*, 2023. 3

[42] Z. Chen, L. Yang, J. H. Lai, and X. Xie. Cunerf: Cube-based neural radiance field for zero-shot medical image arbitrary-scale super resolution. In *Proceedings of the IEEE/CVF International Conference on Computer Vision*, pages 21185–21195, 2023. 3, 5, 6

[43] J. McGinnis, S. Shit, H. B. Li, V. Sideri-Lampretsa, R. Graf, M. Dannecker, and B. Wiestler. Single-subject multi-contrast mri super-resolution via implicit neural representations. In *International Conference on Medical Image Computing and Computer-Assisted Intervention*, pages 173–183, Cham, 2023. Springer Nature Switzerland. 3

[44] H. Kriesel, T. Ropinski, T. Bergner, K. S. Devan, C. Read, P. Walther, and P. Hermosilla. Clean implicit 3d structure from noisy 2d stem images. In *Proceedings of the IEEE/CVF Conference on Computer Vision and Pattern Recognition*, pages 20762–20772, 2022. 3

[45] G. Zhang, X. Li, Y. Zhang, X. Han, X. Li, J. Yu, and Q. Dai. Bio-friendly long-term subcellular dynamic recording by self-supervised image enhancement microscopy. *Nature Methods*, 20(12):1957–1970, 2023. 3, 5

[46] A. Buades, B. Coll, and J. M. Morel. Non-local means denoising. *Image Processing On Line*, 1:208–212, 2011. 3

[47] Marie Farge. Wavelet transforms and their applications to turbulence. *Annual Review of Fluid Mechanics*, 24(1):395–458, 1992. 3

[48] Yulun Zhang, Kunpeng Li, Kai Li, Lichen Wang, Bineng Zhong, and Yun Fu. Image super-resolution using very deep residual channel attention networks. In *Proceedings of the European Conference on Computer Vision (ECCV)*, pages 286–301, 2018. 3

[49] Jiamin Chen, Hirofumi Sasaki, Hsiang-Chieh Lai, et al. Three-dimensional residual channel attention networks denoise and sharpen fluorescence microscopy image volumes. *Nature Methods*, 18:678–687, 2021. 3

[50] J. Lehtinen. Noise2noise: Learning image restoration without clean data. *arXiv preprint arXiv:1803.04189*, 2018. 3

[51] T. Pang, H. Zheng, Y. Quan, and H. Ji. Recorrupted-to-recorrupted: Unsupervised deep learning for image denoising. In *Proceedings of the IEEE/CVF Conference on Computer Vision and Pattern Recognition*, pages 2043–2052, 2021. 3

[52] S. R. Sternberg. Biomedical image processing. *Computer*, 16(1):22–34, 1983. 3

[53] David G. Lowe. Distinctive image features from scale-invariant keypoints. *International Journal of Computer Vision*, 60(2):91–110, 2004. 3

[54] W. Zhao, S. Zhao, Z. Han, X. Ding, G. Hu, L. Qu, and H. Li. Enhanced detection of fluorescence fluctuations for high-throughput super-resolution imaging. *Nature Photonics*, 17(9):806–813, 2023. 3

[55] Kaiming He, Xiangyu Zhang, Shaoqing Ren, and Jian Sun. Deep residual learning for image recognition. In *Proceedings of the IEEE conference on computer vision and pattern recognition*, pages 770–778, 2016. 4

[56] J. Cao, M. K. Wong, Z. Zhao, and H. Yan. 3dmms: robust 3d membrane morphological segmentation of *C. elegans* embryo. *BMC Bioinformatics*, 20:1–13, 2019. 5

[57] A. F. Frangi, W. J. Niessen, K. L. Vincken, and M. A. Viergever. Multiscale vessel enhancement filtering. In *Medical Image Computing and Computer-Assisted Intervention — MICCAI'98: First International Conference Cambridge, MA, USA, October 11–13, 1998 Proceedings 1*, pages 130–137. Springer Berlin Heidelberg, 1998.

[58] X. Huang, J. Fan, L. Li, H. Liu, R. Wu, Y. Wu, and L. Chen. Fast, long-term, super-resolution imaging with hessian structured illumination microscopy. *Nature Biotechnology*, 36(5):451–459, 2018. 5

[59] X. Xu, S. Xu, L. Jin, and E. Song. Characteristic analysis of otsu threshold and its applications. *Pattern Recognition Letters*, 32(7):956–961, 2011. 6

[60] Lin Yen-Chen. Nerf-pytorch. <https://github.com/yenchenlin/nerf-pytorch/>, 2020. 6

- [61] L. Ma, X. Li, J. Liao, Q. Zhang, X. Wang, J. Wang, and P. V. Sander. Deblur-nerf: Neural radiance fields from blurry images. In *Proceedings of the IEEE/CVF Conference on Computer Vision and Pattern Recognition*, pages 12861–12870, 2022. [6](#)
- [62] J. Cao, G. Guan, V. W. S. Ho, M. K. Wong, L. Y. Chan, C. Tang, and H. Yan. Establishment of a morphological atlas of the *C. elegans* embryo using deep-learning-based 4d segmentation. *Nature Communications*, 11(1):6254, 2020. [7](#), [8](#), [9](#)
- [63] A. Domingo-Muelas, R. M. Skory, A. A. Moverley, G. Ardestani, O. Pomp, C. Rubio, and N. Plachta. Human embryo live imaging reveals nuclear dna shedding during blastocyst expansion and biopsy. *Cell*, 186(15):3166–3181, 2023. [7](#), [8](#)
- [64] G. Guan, Z. Li, Y. Ma, P. Ye, J. Cao, M. K. Wong, and Z. Zhao. Cell lineage-resolved embryonic morphological map reveals signaling associated with cell fate and size asymmetry. *Nature Communications*, 16(1):3700, 2025. [9](#)
- [65] K. McDole, L. Guignard, F. Amat, A. Berger, G. Malandain, L. A. Royer, and P. J. Keller. In toto imaging and reconstruction of post-implantation mouse development at the single-cell level. *Cell*, 175(3):859–876, 2018.
- [66] A. Wolny, L. Cerrone, A. Vijayan, R. Tofanelli, A. V. Barro, M. Louveaux, and A. Kreshuk. Accurate and versatile 3d segmentation of plant tissues at cellular resolution. *Elife*, 9:e57613, 2020. [9](#)
- [67] Kaiming He, Georgia Gkioxari, Piotr Dollár, and Ross Girshick. Mask r-cnn. In *Proceedings of the IEEE International Conference on Computer Vision (ICCV)*, pages 2961–2969, 2017. [9](#)
- [68] Michał Chlebiej, Iwona Gorczyńska, Adam Rutkowski, Jan Kluczewski, Tomasz Grzona, Elżbieta Pijewska, and Maciej Szkulmowski. Quality improvement of oct angiograms with elliptical directional filtering. *Biomedical Optics Express*, 10(2):1013–1031, 2019. [9](#)